


Analysis of the seismic wavefield in the Moesian Platform (Bucharest area) for hazard assessment purposes

Journal Article

Author(s):

Manea, Elena F.; [Michel, Clotaire](#) ; Hobiger, Manuel; Fäh, Donat; Cioflan, Carmen Ortanza; Radulian, Mircea

Publication date:

2017-09

Permanent link:

<https://doi.org/10.3929/ethz-b-000173501>

Rights / license:

[In Copyright - Non-Commercial Use Permitted](#)

Originally published in:

Geophysical Journal International 210(3), <https://doi.org/10.1093/gji/ggx254>

Analysis of the seismic wavefield in the Moesian Platform (Bucharest area) for hazard assessment purposes

Elena Florinela Manea,^{1,2} Clotaire Michel,³ Manuel Hobiger,³ Donat Fäh,³ Carmen Ortanza Cioflan¹ and Mircea Radulian¹

¹National Institute of Earth Physics, Calugareni, 12 Magurele, Ilfov, Romania. E-mail: flory.manea88@gmail.com

²Faculty of Physics, University of Bucharest, Atomistilor, 405 Magurele, Ilfov, Romania

³Swiss Seismological Service, Sonneggstrasse 5, ETH Zürich, Zurich, Switzerland

Accepted 2017 June 7. Received 2017 June 6; in original form 2017 January 24

SUMMARY

During large earthquakes generated at intermediate depth in the Vrancea seismic zone, the ground motion recorded in Bucharest (Romania) is characterized by predominant long periods with strong amplification. Time–frequency analysis highlights the generation of low frequency surface waves (<1 Hz) for sufficiently strong and superficial events. This phenomenon has been explained by the influence of both source mechanism (radiation pattern, directivity effects) and mechanical properties of the local geological structure (geological layering and geometry). The main goal of our study is to better characterize and understand the seismic wavefield produced by earthquakes in the area of Bucharest, taking into account its location in the centre of the Moesian Platform, a large sedimentary basin (450 km long, 300 km wide and up to 20 km deep). To this aim, we identify the contribution of different seismic surface waves, such as the ones produced at the edges of this large sedimentary basin or multipath interference waves (Airy phases of Love and Rayleigh waves), on ground motion. The data from a 35 km diameter array (URS experiment) were used. The array was installed by the National Institute for Earth Physics in cooperation with the Karlsruhe Institute for Technology and operated during 10 months in 2003 and 2004 in the urban area of Bucharest and adjacent zones. The earthquake wavefield recorded by the URS array was analysed using the MUSIQUE technique. This technique analyses the three-component signals of all sensors of a seismic array together. The analysis includes 19 earthquakes with epicentral distances from 100 to 1560 km and with various backazimuths with enough energy at low frequencies (0.1–1 Hz), within the resolution range of the array. For all events, the largest portion of energy is arriving from the source direction and the wavefield is dominated by Love waves. The results of the array analyses clearly indicate a significant scattering corresponding to 2-D or 3-D effects of the Moesian Platform. The azimuthal distribution shows that the scattering comes primarily from the southern and northern edges of the basin. The Airy phase of Love waves was clearly identified as the main contributor in the range of the fundamental frequency of resonance of the basin (0.15–0.25 Hz), with directionality along the backazimuth and its opposite direction. Moreover, two further distinct frequency bands around 0.4 and 0.7 Hz with higher amplitudes were identified. Their complex nature is a combination of the higher modes of Rayleigh waves, Airy phases of Love waves and *SH* waves. Love and Rayleigh wave dispersion curves were successfully retrieved by combining the information of all events and show a good match with the ones obtained using ambient vibrations. Additionally, the first higher mode of Rayleigh waves could be retrieved using data from earthquakes. Also, the prograde and retrograde Rayleigh wave ellipticity was computed.

Key words: Earthquake ground motions; Site effects; Surface waves and free oscillations; Wave scattering and diffraction.

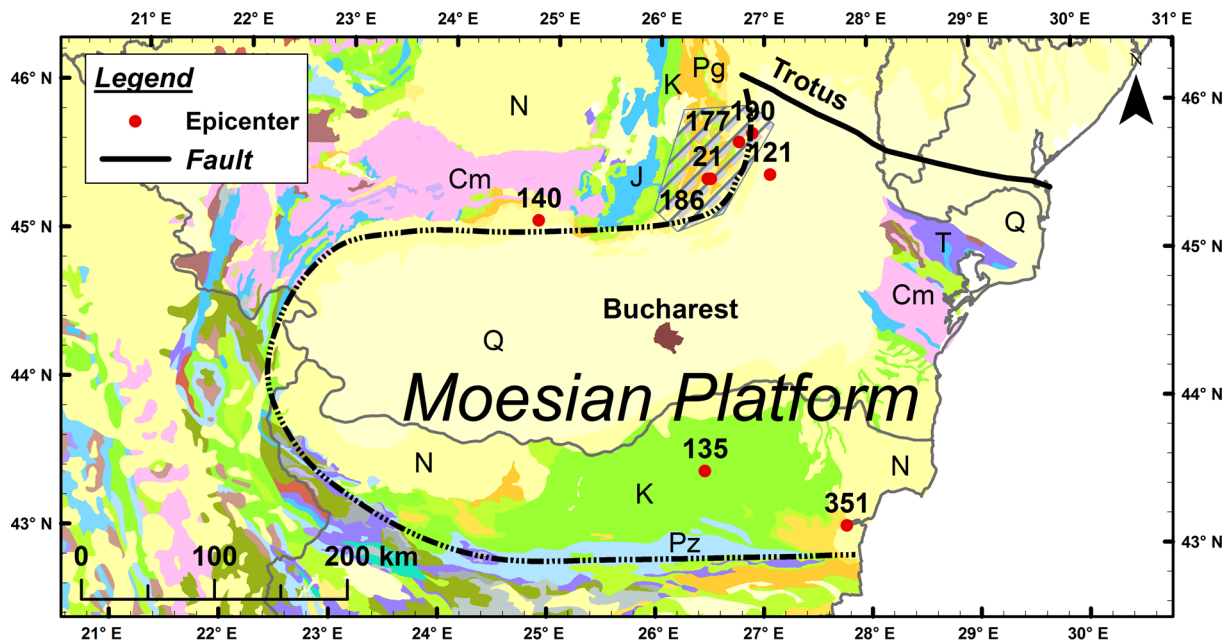


Figure 1. Geological setting of the Moesian Platform (from Asch 2003). The dashed line indicates approximately the limits of the Moesian Platform. The dash polygon encloses the epicentre of the intermediate depth Vrancea earthquakes. Here: Q, Quaternary; N, Neogene; K, Cretaceous; J, Jurassic; Cm, Cambrian; Pg, Palaeogene; Pz, Palaeozoic; T, Triassic. A complete legend of the geological units can be found in Asch (2003).

1 INTRODUCTION

Bucharest is one of the European capitals most affected by earthquakes. It is situated in the Romanian Plain, the central part of the Moesian Platform (Fig. 1). As a consequence of neo-tectonic movements, a syncline structure with a subsidence character was created all over the platform and significant Neogene and Quaternary deposits were accumulated. Bucharest is placed in the axial area of the syncline, where the sedimentary deposits are more than 1000 m thick (Tari *et al.* 1997; Matenco *et al.* 2003).

The earthquakes generated at intermediate depth beneath the bending zone of the southeastern Carpathians (Vrancea region) at about 150 km distance to the north of Bucharest cause persistently great damage over an extended area elongated in the NE–SW direction, and primarily in Bucharest. The Vrancea seismic area is located beneath the southeastern Carpathian Arc bend, at the contact between the East-European plate and the Intra-Alpine and Moesian subplates. An intense seismicity is generated in the mantle, within a narrow almost vertically descending volume between 60 and 180 km depth (Radulian *et al.* 2000). The historical information available for about one millennium indicates an average rate of two to three events with magnitude larger than 7 per century (Radulian *et al.* 2000). Reports in the last six centuries have brought evidence of the particular vulnerability of the city to this type of earthquakes. Basically, two elements have been raised to explain these effects: source and site effects.

Despite the distance from the source, the seismic waves arriving in Bucharest are extremely destructive (Marmureanu *et al.* 2016). On one hand, the propagation at depth is very efficient to the southwest; on the other hand, the unconsolidated uppermost layers of the sedimentary basin underneath Bucharest are amplifying the ground motion (Mândrescu *et al.* 2007). Attempts to simulate the observed strong ground motion in Bucharest area were made using a 2-D hybrid computation algorithm (Fäh *et al.* 1994; Moldoveanu *et al.*

2000; Moldoveanu & Panza 2002; Cioflan *et al.* 2004). They modelled the seismic wave propagation from source to bedrock for a 1-D anelastic model by modal summation, while site effects were taken into account for a 2-D local structure by finite differences. This approach successfully reproduced the recordings for the 1986 ($M_w = 7.1$) and 1990 ($M_w = 6.9$) events, but none of these studies reproduced the distinctive long-period waveforms recorded during the 1977 ($M_w = 7.4$) event.

In large sedimentary basins like the Moesian Platform, the surface waves have a significant contribution to the ground motion, producing strong effects at long periods (Hanks 1975; Takemura *et al.* 2015). Long-period ground motions with dominant periods over 1 s (below 1 Hz) are observed in the Bucharest area (Marmureanu *et al.* 1999).

The enhancement of long periods in the strong ground motion recorded during the major Vrancea earthquakes has been prescribed to ‘the coupling of the incident seismic waves and the deep sedimentary layers, which in this way becomes resonant’ (Grecu *et al.* 2003). The fundamental frequency in the Bucharest area lies between 0.14 and 0.29 Hz (3–7 s) and is interpreted as corresponding to the interface between Neogene and Cretaceous geological units, whose distribution confirms that the bedrock is dipping to the north at about 1.4 km depth (Manea *et al.* 2016).

Other factors which can play an important role, causing such strong seismic ground motion are: (1) source location, which influences the angle, azimuth and type of incident waves (Moldoveanu & Panza 2002); (2) strong lateral heterogeneities in the superficial sediments (Panza *et al.* 2002); (3) surface waves generated at the edge of the basin, producing large amplitudes of later phases arriving after the direct *S* wave (Field 1996; Chávez-García *et al.* 1999; Joyner 2000; Lebrun *et al.* 2002; Cornou & Bard 2003; Roten *et al.* 2008); (4) nonlinear behaviour of the sediments (Marmureanu *et al.* 1999; Balan *et al.* 2011).

The goal of this study is to characterize and interpret the 3-D seismic wavefield in the Bucharest area. We are interested in identifying the contribution of the different types of surface waves and how they are generated. A particular interest lies on the contribution of the waves produced at the edges of this large sedimentary basin and on multipath interference waves (Airy phases of Love and Rayleigh waves) in the ground motion.

Therefore, we looked for the energy distribution of the wavefield with respect to time, frequency and azimuth, first for the whole wavefield (time–frequency analysis) and then decomposing the surface waves by type. In order to perform the wavefield decomposition, the MUSIQUE technique (Hobiger *et al.* 2012, 2016) was applied. This method is a combination of the ‘classical’ MUSIC (Schmidt 1986) and the quaternion-MUSIC (Miron *et al.* 2006a,b) algorithms. In the computation, the three-component signals are used and allow us to estimate the azimuth and energy contributions of the Love and Rayleigh waves and to distinguish between retrograde and prograde Rayleigh wave particle motion. The basic principle of MUSIC is to separate the signal and noise subspaces and then to estimate the signal parameters. When using the quaternion formulation of the quaternion-MUSIC algorithm, the phase information and the sense of rotation of the particle motion are naturally preserved allowing the distinction between retrograde and prograde Rayleigh wave motion (Imtiaz *et al.* 2014). Successfully applied to data from the San Jose Dense Seismic array in the Santa Clara Basin (Hobiger *et al.* 2016) and the Argostoli array in Greece (Imtiaz *et al.* 2014), this method is used in this paper in the sedimentary basin outside of the Carpathian Mountains (Romania).

The analysis includes 19 regional earthquakes with $M_w > 3$ that have enough energy at low frequency (0.1 – 1 Hz), recorded by the Urban Experiment array (URS, Ritter *et al.* 2005), a temporary array of 31 stations with 35 km aperture.

After presenting the used techniques and the data set, we show the results of the time–frequency analysis. Then, the MUSIQUE results are shown, notably the dispersion curves of Love and Rayleigh waves and the ellipticity of Rayleigh waves, the distribution of Love and Rayleigh waves at different frequencies and the azimuthal distribution of the waves.

2 METHODS

2.1 Time–frequency analysis

A first method to help understanding the content of the earthquake wavefield is the time–frequency analysis. It allows us to observe the generation of surface waves close to the resonance frequencies of the basin. For that purpose, we used the smoothed pseudo-Wigner–Ville distribution (Wigner 1932; Ville 1948) implemented in the Matlab time–frequency toolbox (Auger & Flandrin 1995). Moreover, in order to enhance the resonance frequencies, also after the strongest phases of the signal, we made the signal stationary by dividing it by its envelope before computing the smoothed pseudo-Wigner–Ville distribution as proposed by Michel & Guéguen (2010) for earthquake recordings in buildings.

2.2 MUSIQUE algorithm

The MUSIQUE algorithm (Hobiger 2011; Hobiger *et al.* 2011, 2016) was used to characterize and interpret the seismic wavefield in Bucharest. This algorithm consists of a combination of the classical MUSIC algorithm (Schmidt 1986) and the quaternion-MUSIC

algorithm (Miron *et al.* 2006a,b). MUSIQUE analyses the three-component signals of all sensors of a seismic array together. The analysis is performed for each frequency separately.

First, the signals are filtered with a small-band Chebyshev filter around the desired frequency. Then, the signals are cut into time windows of the length of several periods, resulting in a larger number of time windows for high frequencies than for low frequencies.

Each time window is first analysed using the ‘classical’ MUSIC algorithm (Schmidt 1986), which is based on the separation of signal and noise subspaces. If the array is composed of N three-component seismic sensors, their respective data at frequency f can be stored in three complex data vectors $X_l(f)$ of size $N \times l$, where $l = 1$ stands for the vertical, $l = 2$ for the eastern and $l = 3$ for the northern component.

For each component, a covariance matrix $S_l(f)$ of size $N \times N$ is computed by

$$S_l(f) = E(X_l(f) X_l^H(f)). \quad (1)$$

Here, $E()$ denotes the mathematical expectation value and H denotes the conjugate transpose of a matrix. A single covariance matrix $S(f)$ is formed by summing the covariance matrices of the different components. The eigenvectors and eigenvalues of $S(f)$ are calculated. The eigenvectors associated with the largest eigenvalues span the signal subspace. The remaining eigenvectors span the noise subspace G . The maximization of the MUSIC functional

$$P(k) = \frac{1}{\mathbf{a}^H(k) G G^H \mathbf{a}(k)} \quad (2)$$

yields the wave vector k of the most energetic wave arrival. In eq. (2), \mathbf{a} is the steering vector defined by

$$\mathbf{a}(k) = \frac{\exp(-i R k)}{\sqrt{N}}. \quad (3)$$

The steering vector is the vector which indicates the theoretical phase delays for the different stations of the array located at the sensor positions R for the propagation of a wave with wave vector k defined by

$$k = -2\pi f s (f) (\sin\vartheta, \cos\vartheta, 0)^T, \quad (4)$$

where ϑ is the backazimuth and s is the slowness of the wave. A 2-D grid search yields the parameters ϑ and s which maximize $P(k)$. The radial and transverse components of the horizontal particle motion are separated by projecting the horizontal signals in the identified direction ϑ :

$$X_{\text{radial}} = -\sin\vartheta X_2 - \cos\vartheta X_3, \quad (5)$$

$$X_{\text{transverse}} = \cos\vartheta X_2 - \sin\vartheta X_3. \quad (6)$$

By summing the squared signals of the respective components for all sensors of the array, the total energies of the vertical, radial and transverse components in the respective time window are calculated. In this study, the proportionality factor for the conversion of velocity to energy is not taken into account, because our interest lies in the relative energies.

The identification of Love and Rayleigh waves is based on the energies. If the transverse component carries more energy than the radial and vertical components together, the wave is identified as a Love wave and the processing is stopped here. In the opposite case, it is considered as a possible Rayleigh wave and its polarization parameters are determined in the following processing step.

For Rayleigh waves, the polarization between the radial and vertical components is of major interest. Here, it is estimated by the

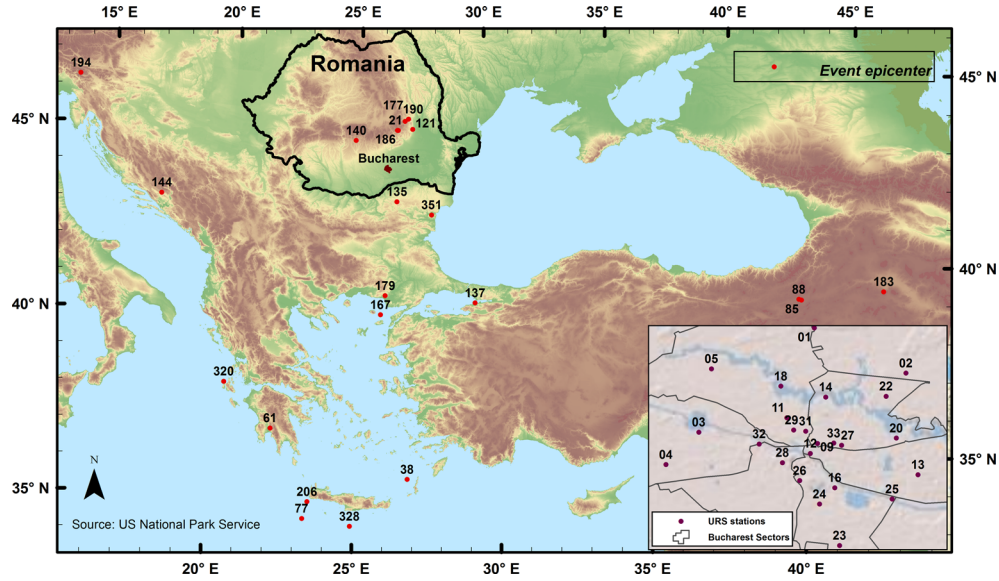


Figure 2. Localization of the analysed earthquake epicentres (red dots). Location of the URS stations in Bucharest and adjacent areas is plotted in the inset. URS20 is a permanent station of the Romanian strong-motion network.

quaternion-MUSIC algorithm (Miron *et al.* 2006a,b), which is applied to the radial and vertical components. The processing is based on quaternions, hypercomplex numbers of dimension 4 (e.g. Ward 1997). We refer to Hobiger *et al.* (2016) for a more detailed introduction in the quaternion algebra of the MUSIQUE algorithm and only give the basic idea here. The basic concept is that quaternions are an extension of complex numbers. Instead of a single imaginary unit i , there are three different imaginary units i, j and k which satisfy

$$i^2 = j^2 = k^2 = ijk = -1. \quad (7)$$

The advantage of using the quaternion formulation is that we can store the two complex data matrices for the radial and vertical components in a single quaternion-valued data matrix. The polarization properties of the signal remain naturally preserved in the data. The quaternion data matrix $X_q(f)$ is formed by

$$X_q(f) = \text{Re}(X_{\text{vertical}}(f)) + i \text{Re}(X_{\text{radial}}) + j \text{Im}(X_{\text{vertical}}) + k \text{Im}(X_{\text{radial}}). \quad (8)$$

The quaternion-valued covariance matrix $S_q(f)$ is built in analogy to eq. (1). The quaternion-MUSIC functional is analogue to eq. (2), but the expression of the steering vector is changed to

$$a_q = \frac{[\cos \rho + i \sin \rho \exp(j\varphi)] \exp(-jRk)}{\sqrt{N}}, \quad (9)$$

where φ is the phase difference between the vertical and radial components and ρ is the amplitude parameter. The ellipticity is then given by $\tan \rho$.

In the original quaternion-MUSIC algorithm (Miron *et al.* 2006a,b), the four parameters backazimuth ϑ , slowness s , phase difference φ and amplitude parameter ρ are identified by a 4-D grid search, which is a time-consuming task. Anyhow, in our case, the backazimuth and slowness values were already determined in the first step of the code. In this case, the two remaining parameters can be determined analytically (Hobiger 2011).

The interpretation of the polarization parameters is simple. In theory, the phase shift φ is 90° for retrograde Rayleigh waves and 270° for prograde waves. In order to account for possible measurement and estimation errors, all waves with phase shifts between 45° and 135° are identified as retrograde Rayleigh waves and all waves with phase shifts between 225° and 315° as prograde Rayleigh waves. All other waves are left unclassified.

For every time window, the total energy is calculated as the sum of the energies of all components and all stations of the array. The sum of the transverse energies of all stations of the array is taken as the Love wave energy if the dominant wave is identified as a Love wave. If the dominant wave is identified as a Rayleigh wave, the Rayleigh wave energy is taken as the sum of the horizontal and vertical energies of all stations.

As a byproduct of this analysis, the velocity distribution with respect to the frequencies of the retrieved waves can be analysed in order to determine the dispersion curve of the Rayleigh (prograde and retrograde) and Love waves for fundamental and higher modes (Hobiger *et al.* 2016). Similarly, the ellipticity curve of the Rayleigh waves can be retrieved.

3 DATA

In the framework of the URS Project, 31 seismic stations (broadband velocity sensors) were installed in Bucharest and the adjacent areas by the National Institute for Earth Physics in cooperation with the Karlsruhe Institute of Technology (Ritter *et al.* 2005). The stations recorded continuously and simultaneously from October 2003 to August 2004 (Fig. 2). In this period, 4 seismic events with $M_w > 4$, 48 seismic events with $M_w > 3$ and 67 seismic events with $M_w > 2$ occurred in the Vrancea area as well as more than 75 worldwide events with $M_w > 4.5$ that were recorded on the array. In this study, 19 earthquakes with a good signal-to-noise ratio from this data set and 3 large earthquakes recorded by a single station in Bucharest are used (Table 1 and Fig. 2). The data were processed by removing the linear trend, correcting for the instrument response

Table 1. List of analysed earthquakes with their respective parameters that were obtained from the NIEP (*, site: <http://www1.infp.ro/arhiva-in-timp-real>) and from the EMSC (<http://www.emsc-csem.org/Earthquake/>) catalogues. Three events are only recorded at a single station in Bucharest: 177, 186 and 190.

Event ID	Date (yyyy/mm/dd)	Time	Magnitude (M_w)	Latitude ($^{\circ}$ N)	Longitude ($^{\circ}$ E)	Depth (km)	Backazimuth ($^{\circ}$)	Epicentral distance (km)	Location
21	2004/01/21	05:49	4.1	45.52	26.46	118	14	125	Romania*
38	2004/02/07	21:17	5.1	35.83	26.86	9	176	955	Crete
61	2004/03/01	00:35	5.2	37.16	22.1	10	201	872	Greece
77	2004/03/17	05:21	6.1	34.69	23.31	40	192	1105	Crete
85	2004/03/25	19:30	5.7	39.95	41.06	40	117	1321	Turkey
88	2004/03/28	03:51	5.6	39.98	40.97	9	117	1321	Turkey
121	2004/04/30	09:19	3.2	45.55	27.06	20	32	147	Romania*
135	2004/05/14	11:09	3.1	43.54	26.45	3	163	101	Bulgaria*
137	2004/05/16	03:30	4.3	40.71	29.33	10	148	490	Turkey
140	2004/05/19	22:37	3.3	45.22	24.84	0	312	134	Romania*
144	2004/05/23	15:19	5	43.41	17.5	10	258	670	
167	2004/06/15	12:02	5.2	40.4	25.88	5	182	446	Aegean
179	2004/06/27	03:31	4.5	40.93	26.04	8	181	400	Greece
183	2004/07/01	22:30	5.2	39.78	43.96	21	115	1561	Turkey
194	2004/07/12	13:04	5.2	46.36	13.76	11	278	989	Austria
206	2004/07/24	19:00	4.7	35.16	23.47	10	191	1051	Crete
320	2003/11/16	07:22	5.1	38.37	20.38	10	213	823	Greece
328	2003/11/24	15:51	5.2	34.51	24.92	26	185	1104	Crete
351	2003/12/17	23:15	4.1	43.17	27.77	10	146	201	Bulgaria*
177	1977/03/04	19:21	7.4	45.77	26.76	94	21	158	Romania*
186	1986/08/30	21:28	7.1	45.52	26.49	131	15	126	Romania*
190	1990/05/30	10:40	6.9	45.83	26.89	91	22	169	Romania*

and filtering by a band pass with four poles between 0.01 and 10 Hz. Time–frequency analysis was first computed for five events (021, 177, 186, 190 and 351) at URS 20 station (see Fig. 2), the permanent station of the Romanian strong motion Network in Bucharest. The signals of the 19 selected events recorded by the URS array have then been analysed using MUSIQUE for 100 different frequency values between 0.1 and 1 Hz, using a logarithmic frequency scale.

4 RESULTS

4.1 Time–frequency analysis of earthquake recordings

We first look at waveforms and at the time–frequency distribution of the recordings of five example earthquakes (events 21, 177, 186, 190 and 351) to observe the similarities and differences in the generation of surface waves at the resonance frequencies of the basin in Bucharest. For the first event (Fig. 3, left), an intermediate-depth event that occurred in the Vrancea area (021), the energy is distributed between 0.5 and 6 Hz and is not generating surface waves due to the large focal depth (Sèbe *et al.* 2009). Conversely, for the regional shallow event located on Bulgarian territory (351), surface waves at low frequencies strongly dominate the signal (Fig. 3, right).

A zoom in the frequency range between 0.01 and 1 Hz using the stationary signal (Fig. 4) shows that three particular frequency ranges are excited alternatively due to the energy trapped in the basin: the frequency bands around the fundamental frequency of the basin at about 0.16 Hz, around a peak at 0.4 Hz and another one related to the resonance of Quaternary layers around 0.7 Hz (0.6–0.9 Hz, Manea *et al.* 2016). Similar energy patterns can be seen for the three large intermediate-depth events with a predominant frequency around 0.6–0.8 Hz, while Grecu *et al.* (2003) assume that the predominant frequency of Vrancea earthquakes with $M_w > 7$ is

0.5–1 Hz. The spectrogram of these events is dominated by the energy of body waves. The apparently increasing frequency for event 351 corresponds to the arrival of the direct dispersive surface waves probably refracted at the southern basin edge considering their frequencies. The energy of reflected surface waves in the basin can be seen after 130 s for this event. It is therefore of relevance to understand how these surface waves are generated using a method decomposing the wavefield.

4.2 Surface wave dispersion and ellipticity

The multimodal dispersion characteristics of the Rayleigh and Love waves were retrieved using the MUSIQUE algorithm. They are used to validate previously published velocity models for further interpretations and also show the energy distribution between the fundamental and higher modes and between retrograde and prograde Rayleigh waves. For a single event, the dispersion curve cannot be well retrieved. Therefore, the energy distributions for all events recorded by the array (Table 1) were stacked to retrieve the Love and Rayleigh wave dispersion curves of the fundamental and higher modes (Fig. 5). For this stacking, the recordings of the respective events were normalized by their total recorded energy. The comparison with the Love wave dispersion curves obtained from ambient vibrations (Manea *et al.* 2016) and with the ones proposed by Sèbe *et al.* (2009) shows a good agreement (Fig. 5 left). The dispersion curves from ambient vibrations were retrieved using the three-component frequency-wavenumber analysis (Fäh *et al.* 2008; Poggi & Fäh 2010). The fundamental mode dispersion curve of Love waves that Sèbe *et al.* (2009) measured was retrieved from eight teleseismic events recorded by the URS array using a modified frequency-wavenumber analysis with non-uniform wave velocities. Using MUSIQUE, we can also retrieve the dispersion

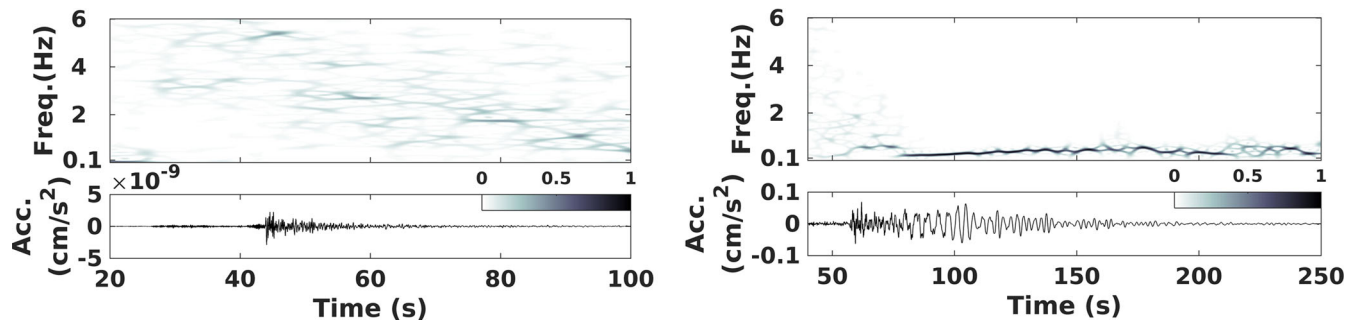


Figure 3. Time–frequency analysis of the eastern component of the URS20 station for the recording of the Vrancea event 021 ($M_w = 4.1$, $h = 117.7$ km, 125 km epicentral distance, left side) and of the Bulgaria event 351 ($M_w = 4.1$, $h = 10$ km, 201 km epicentral distance, right side). The colour bar represents the normalized energy.

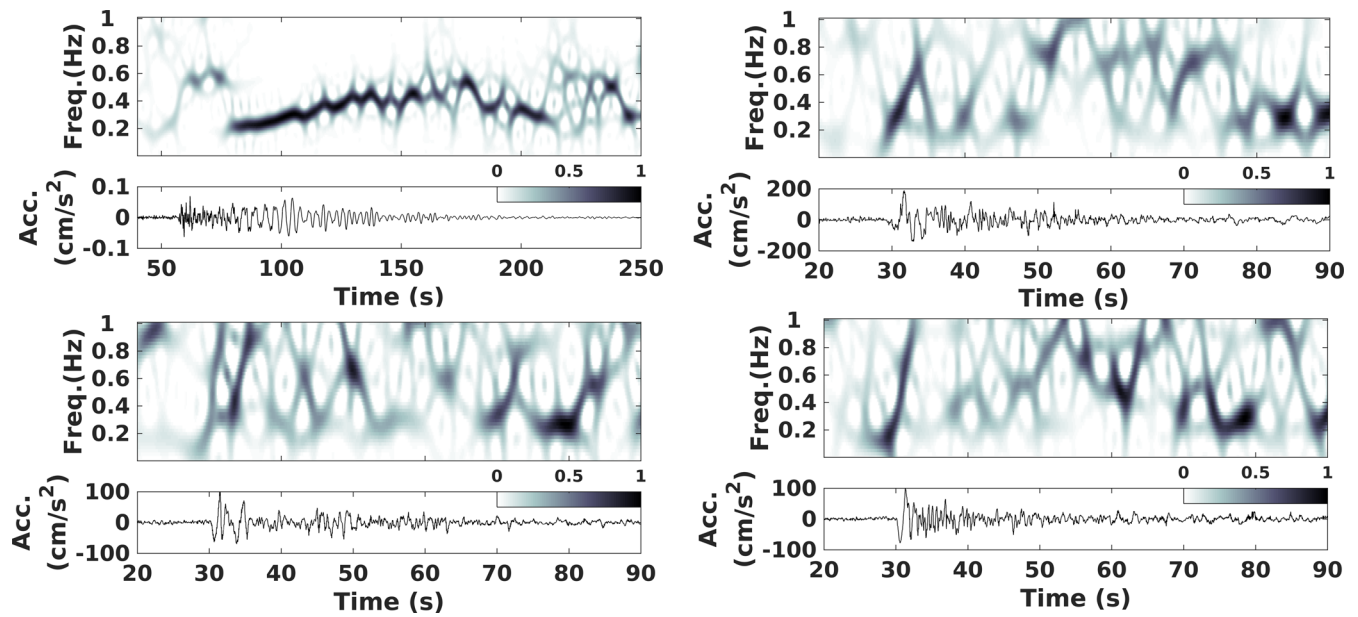


Figure 4. Time–frequency analysis of the stationary signal in the frequency range between 0.01 and 1 Hz for the eastern component of station URS20 for four events that occurred in Bulgaria (351, top left) and in the Vrancea area (177, top right; 186, bottom left; 190, bottom right). The colour bar represents normalized energy. Note that the Vrancea recordings are shorter than the 351 event and do not show the complete surface waves window.

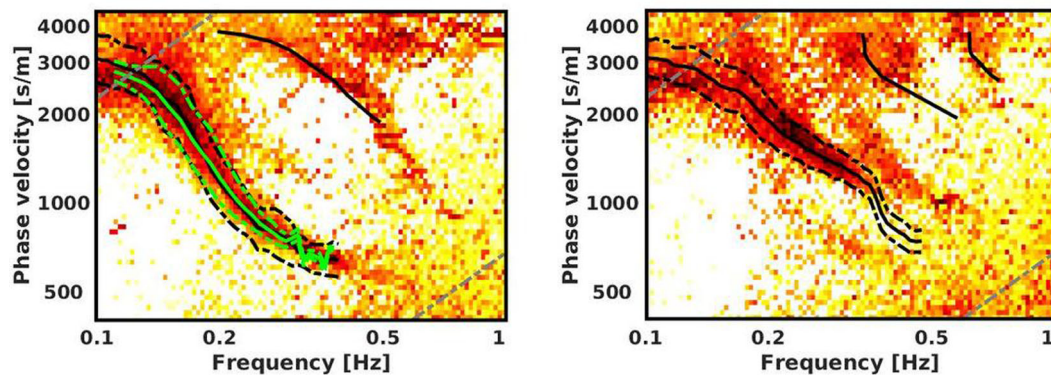


Figure 5. Comparison between the Love (left) and Rayleigh (right) wave dispersion curves obtained from MUSIQUE (background), the dispersion curves from the three-component frequency–wavenumber analysis of ambient vibrations (Manea *et al.* 2016; solid black lines) and the dispersion curves from Sèbe *et al.* (2009; green lines). The dashed black lines are the standard deviations of the fundamental-mode dispersion curve and the dashed grey lines are the upper and lower resolution limits of the URS array.

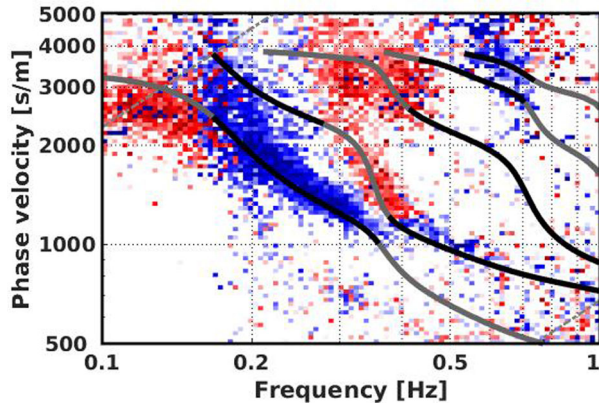


Figure 6. Comparison between the Rayleigh wave dispersion curves (red: retrograde waves; blue: prograde waves) obtained from MUSIQUE (background) and the theoretical dispersion curves (grey lines: retrograde and black lines: prograde waves) modelled for the velocity model of Bucharest by Manea *et al.* (2016). The dashed lines are the resolution limits of the URS array.

curve for frequencies above 0.4 Hz for the fundamental and higher modes.

The density distributions of Rayleigh waves obtained using MUSIQUE and their comparison with the Rayleigh wave dispersion curves obtained from ambient vibrations are displayed in the right panel of Fig. 5. The density distributions of prograde and retrograde Rayleigh waves were combined to better identify the modes. A comparison with the theoretical dispersion curves computed from the regional velocity model obtained from ambient vibrations (Manea *et al.* 2016) shows a good fit with the dispersion re-

trieved with MUSIQUE for prograde and retrograde Rayleigh waves (Fig. 6). This velocity profile was obtained from a joint inversion of Love and Rayleigh wave dispersion curves (fundamental and higher modes), H/V peak and Rayleigh wave ellipticity from ambient vibrations and constrained by superficial velocity models from borehole data. Using earthquakes, the first higher mode of Rayleigh waves can be identified although it was not visible using ambient vibrations. It shows a good match with the theoretical curve computed from the regional velocity model. Fig. 6 clearly shows the partition of the modes into prograde and retrograde waves, both for the observations and the theoretical model. The fundamental mode is retrograde at low frequencies and becomes prograde above 0.17 Hz. The first higher mode is retrograde below 0.4 Hz and changes to prograde above. This means that the ellipticity curve has singularities at the respective frequencies, which is only the case if the shear-wave velocity profile has a well-pronounced velocity contrast. The second higher mode of Rayleigh waves is characterized partially by retrograde waves and the third one by prograde waves.

The Rayleigh wave ellipticities for prograde and retrograde waves were also estimated and compared to the theoretical ellipticity computed from the 1D regional velocity model (Manea *et al.* 2016). The comparison with the H/V curve from ambient vibrations (Manea *et al.* 2016) shows that the right flanks of the peaks are dominated by the prograde waves and the left flanks by retrograde waves as predicted by the theory (Fig. 7). This is particularly the case for the fundamental mode that shows a change in the sense of rotation at its peak value (0.17 Hz) that matches well the theoretical ellipticity.

The observed ellipticity peak at 0.4 Hz, corresponding to a change of particle motion from retrograde to prograde, corresponds to the first harmonic mode as modelled with the regional velocity model that has a peak at 0.38 Hz (Fig. 7). This peak is not observed in

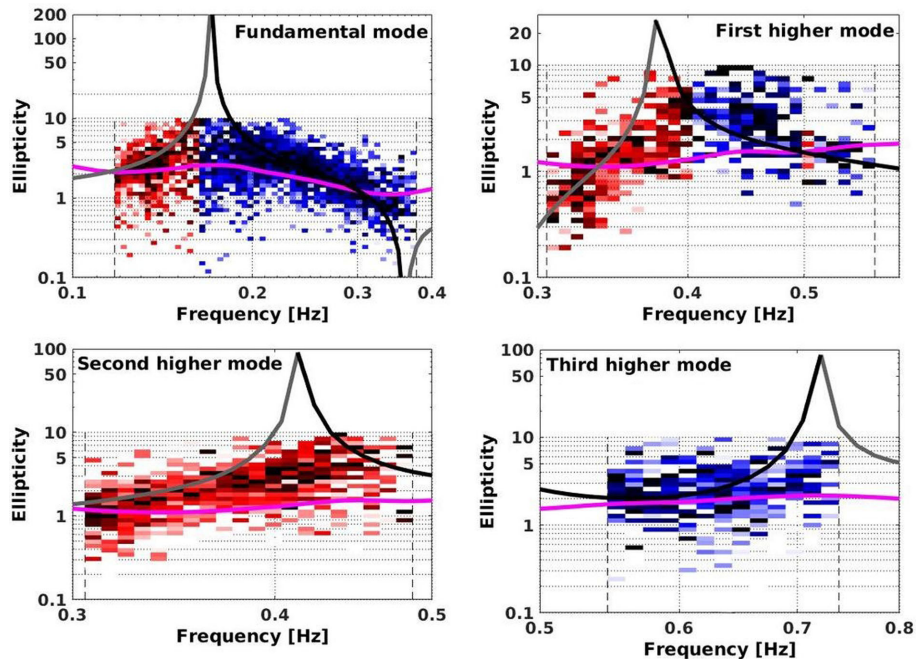


Figure 7. Comparison between the Rayleigh wave ellipticity curves (retrograde waves, red colour; prograde waves, blue colour) obtained from MUSIQUE (background) and the theoretical ellipticity curves (grey lines, retrograde waves; black lines, prograde waves) modelled for the velocity model of Bucharest (Manea *et al.* 2016). The magenta curve is the H/V ratio computed from ambient vibration (Manea *et al.* 2016). The dashed vertical black lines show the frequency ranges where each mode is addressed.

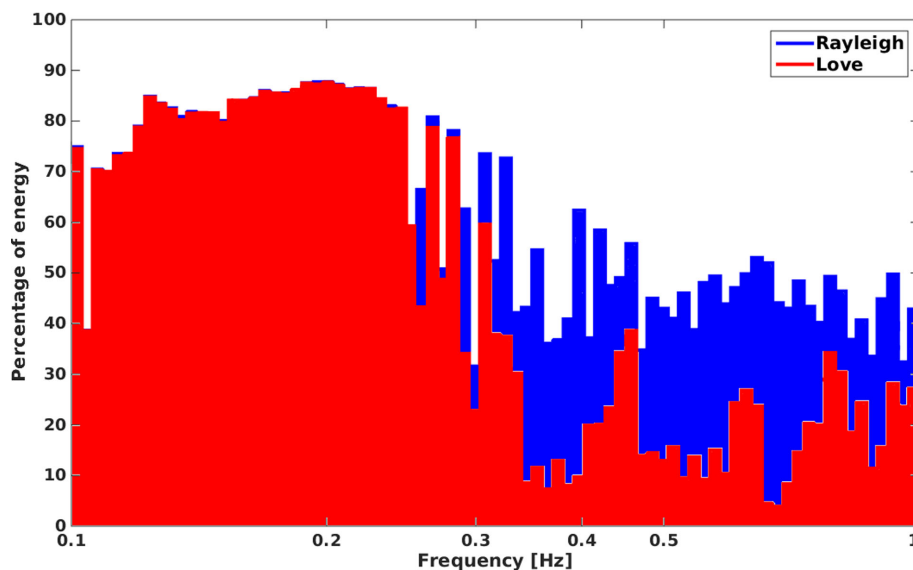


Figure 8. Distribution of the analysed energy in different frequency bands that is carried by identified Love and Rayleigh waves (event 351).

the H/V ratios from ambient vibrations. Manea *et al.* (2016) already showed that ambient vibrations do not contain energy at the first higher mode of Rayleigh waves.

The decomposition of the wavefield shows the presence of another mode of Rayleigh waves that can be seen as retrograde waves only. An ellipticity peak may be present at about 0.5 Hz but, unfortunately, the prograde waves are not identified. This peak probably corresponds to the second harmonic mode of Rayleigh waves as it can also be observed from the dispersion plot (Fig. 6). Both ellipticity and dispersion curves match with the theoretical values from the regional model, although the ellipticity peak is slightly shifted towards higher values than predicted (0.43 Hz). This peak is not clearly observed in the H/V ratios from ambient vibrations, though a small bump can be seen in the curve at 0.44 Hz (Fig. 7).

The predominant peak around 0.7 Hz (0.6–0.9 Hz) that was observed in the H/V curves from the ambient vibration data (Bonjer *et al.* 1999; Manea *et al.* 2016) corresponds to the peak of the third mode of the Rayleigh wave ellipticity from the regional model (Fig. 7). Manea *et al.* (2016) also observed this peak in the SH transfer function (SH -wave resonance) but it is not successfully retrieved using MUSIQUE technique (Figs 6 and 7).

These successful comparisons confirm that the velocity model of Manea *et al.* (2016) is mostly reproducing the observed data. It can be further used for seismic hazard estimation at local scale and can be also improved with new information.

4.3 Energy distribution between Love and Rayleigh waves

The MUSIQUE algorithm allows us to understand the partitioning of seismic energy between Love and Rayleigh waves. Fig. 8 shows this distribution for event 351 ($M_w = 4.1$), located at 201 km distance from the URS array to the southeast. Love waves dominate the seismic wavefield below 0.25 Hz (about 80 per cent of the analysed energy). Above 0.35 Hz, Rayleigh waves are more prominent. Since the fundamental resonance frequency of the basin is between 0.14 and 0.25 Hz (Manea *et al.* 2016), the energy around this resonance frequency is dominated by Love waves. The H/V curve from ambient vibrations is also strongly influenced by Love waves, and therefore

is not matching the obtained Rayleigh wave ellipticity in Manea *et al.* (2016). The observed energy around the resonance frequency at 0.7 Hz in the time–frequency analysis is, on the contrary, a mix of Rayleigh and Love waves contributing about 50 per cent of the total energy. It should be noted that about half of the wavefield above 0.35 Hz remains unexplained by surface waves according to the MUSIQUE method or belong to the non-dominant wave type at their respective time window. These patterns can be similarly observed for all events creating surface waves.

For the example event, the azimuth distribution of the Love waves shows two main directions of arrival at the array (Fig. 9): between 130° and 180° and between 280° and 360° . The first corresponds to waves coming from the backazimuth of the earthquake (direct waves). In the second case, the coming waves are interpreted as surface waves reflected by the northern edge of the basin. For the Love waves, the direct waves arrive from directions slightly deviated from the backazimuth, probably due to refraction at the southern edge of the basin. Below 0.35 Hz, all Rayleigh waves come from the event's backazimuth and are mainly prograde (Fig. 10).

During large earthquakes, the low group velocity of Love waves controls the overall duration and amplitude at the free surface in large sedimentary basins (Frankel *et al.* 2001). These waves are partly responsible for generating the large amplification (Olsen *et al.* 2006). In order to have a better understanding of the origin of these phases of Love and Rayleigh waves in the wavefield recorded in Bucharest, the group velocity was computed for the regional geological structure proposed by Manea *et al.* (2016). The result is shown in Fig. 11.

The group velocities of Love and Rayleigh waves show several minima corresponding to their Airy phases: around these frequencies, the wave packets will superimpose to generate large amplitudes (Konno & Ohmachi 1998). The local minimum on the fundamental mode of Love waves is around the fundamental frequency of the regional model (0.16 Hz) and for the higher modes around 0.4 and 0.7 Hz. These Love wave Airy phases travel in the basin with a group velocity between 400 and 500 m s⁻¹ and they can be seen in Fig. 8 as bands with increased Love wave energy. All modes of Rayleigh waves produce two minima in the group velocity each. The first local minima of the fundamental and the first higher modes occur

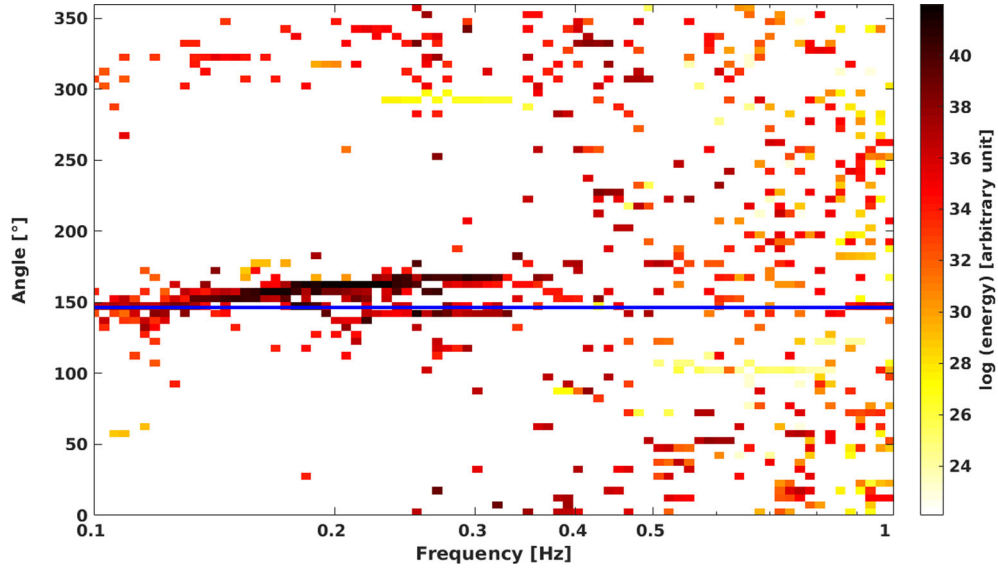


Figure 9. Backazimuth distribution of Love waves for different frequency ranges (event 351). The colour scale shows the normalized energy and the blue line indicates the backazimuth of the event.

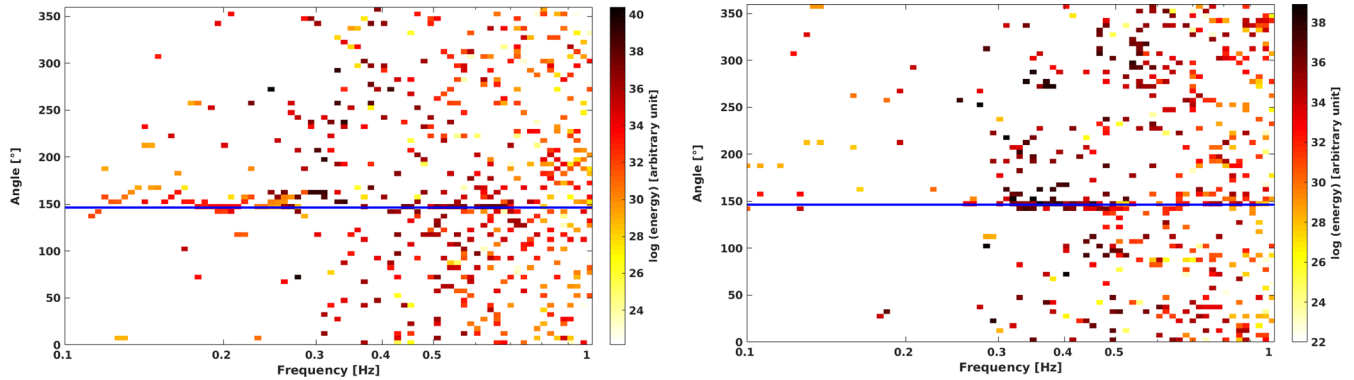


Figure 10. Backazimuth distribution of prograde (left) and retrograde (right) Rayleigh waves for different frequencies (event 351). The colour scale shows the normalized energy and the blue line indicates the backazimuth of the event.

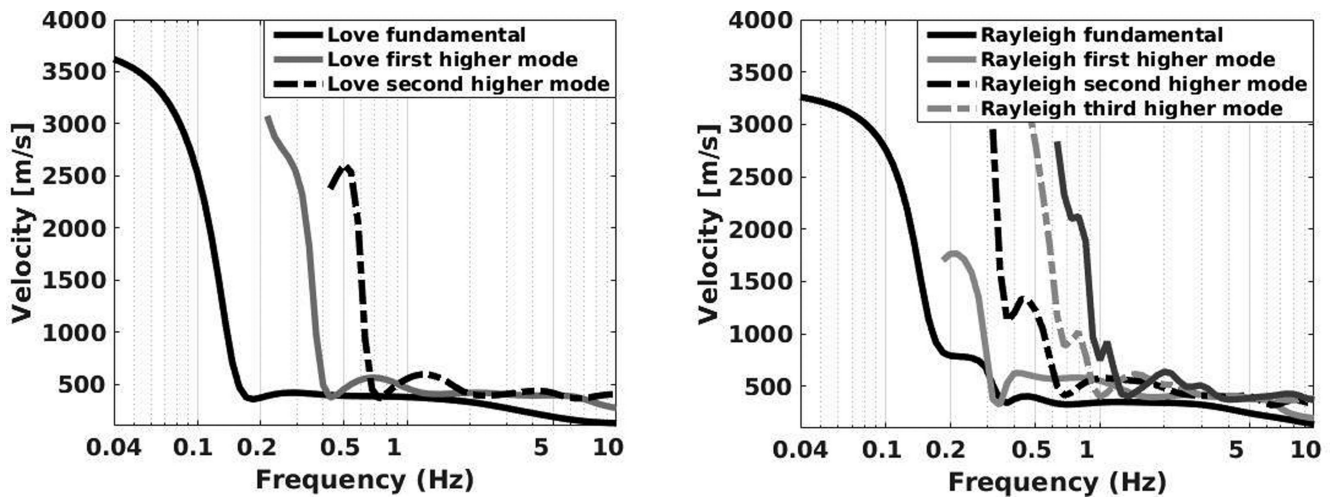


Figure 11. The group velocity of Love waves (left) and Rayleigh waves (right) computed for the regional velocity profile of Bucharest (Manea *et al.* 2016).

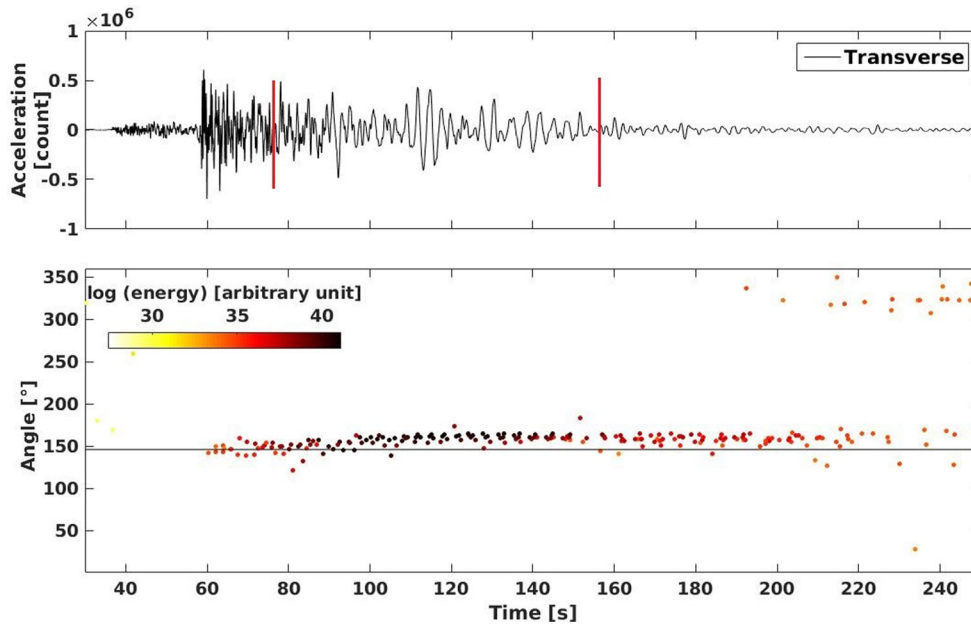


Figure 12. Time–angle analysis for event 351 (transverse component) in the frequency range between 0.14 and 0.25 Hz. The red lines in the seismogram show the time window where the direct surface waves are strongest.

at the same frequency (0.4 Hz). Their minimum group velocity is also close to 400 m s^{-1} .

To identify the Airy phases of the fundamental mode of Love waves in the earthquake, a bandpass filter around the fundamental frequency (0.15–0.25 Hz) was applied to the transverse component of the recording for event 351 at station URS20, obtained by rotating the horizontal components with respect to the backazimuth of the event (Fig. 12). A group of Love waves can be identified (Fig. 12) between 60 and 160 s coming at the array along the backazimuth direction. A second directivity was observed from the opposite of the backazimuth. Although the waves are coming late at the network, they can have a significant impact on the ground motion in case of large earthquakes. A similar filter between 0.5 and 0.7 Hz for prograde and between 0.3 and 0.55 Hz for retrograde Rayleigh waves, that correspond to the local minima of the Rayleigh waves (Fig. 11, right), was applied but no group of waves arriving from a particular direction could be observed.

4.4 Azimuthal energy distribution and scattered wave directions

The wavefield was analysed in four frequency ranges: 0.1–0.15 Hz, 0.15–0.25 Hz (fundamental frequency of the site), 0.25–0.55 Hz and 0.55–1 Hz. The azimuthal energy distribution in different frequency ranges for event 351 can be seen in Fig. 13. In the frequency range between 0.1 and 0.15 Hz, below the fundamental frequency, the wavefield is described by Love waves arriving at the array which are only slightly influenced by the basin due to their larger wave lengths (see also dispersion curves in Fig. 5). Between 0.15 and 0.25 Hz, the energy comes mainly from the source direction and the wavefield is dominated by Love waves. In the frequency range from 0.25 to 0.55 Hz, some energy comes from the opposite of the backazimuth. The energy arriving from the basin edges is less significant than the one that comes from the source direction. In the frequency range between 0.55 and 1 Hz, the wavefield is character-

ized by prograde Rayleigh waves arriving from the source direction and by Love waves from the northeastern edge of the basin.

The results for the other events are given in the Supporting Information. For all events, the energy arrives diffracted from the theoretical backazimuth with a high amount of Love waves around the fundamental frequency of resonance due to the reflection/refraction of the incident waves with different geophysical interfaces, especially the lateral basin edges. Other wave directions are well defined as the ones coming from the opposite direction of the backazimuth of these events (reflected waves on the basin edge) with a relevant contribution to the seismic wavefield.

To identify and interpret the scattered waves in the basin for all events, the energy arriving from within $\pm 40^\circ$ of the theoretical backazimuth has been removed and the results for all earthquakes were stacked, using the same normalization as for the dispersion curves (Fig. 14).

In the frequency range of 0.10–0.15 Hz, the wavefield is dominated by Love waves that arrive with a considerable amount of energy from the southern edge of the basin, especially for events located North of Bucharest. Around the fundamental frequency (0.15–0.25 Hz), the wavefield is also characterized by Love waves reflected on the southern edge for the same events. The waves in this frequency range represent the largest contribution of scattered waves in terms of energy. Between 0.25 and 0.55 Hz, the northern edge of the basin (Carpathian Mountains) plays an important role and the waves arriving from this direction dominate the wavefield. Those do not depend on the location of the source. Above 0.55 Hz, there is not much energy in the scattered wavefield. The wavefield is more complex with waves arriving from all angles.

5 DISCUSSION

From the analysis of the wavefield, three particular frequencies can be observed. The first one is around 0.25 Hz and corresponds to the fundamental frequency of the basin. Around this frequency, the wavefield is dominated by the Airy phase of Love waves, although

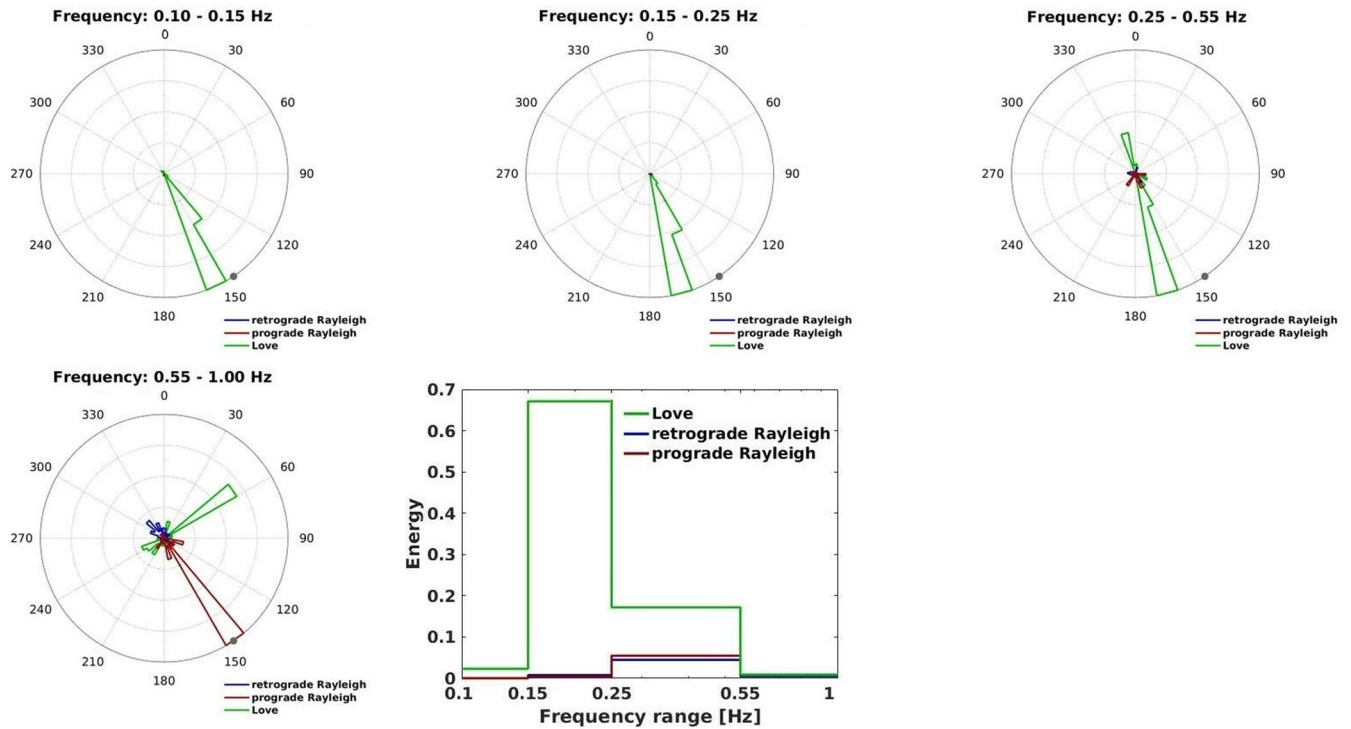


Figure 13. Azimuthal energy distribution for different frequency ranges for event 351. The grey dot indicates the theoretical backazimuth of the event. In each frequency range, all curves were normalized to the maximum. The figure on the bottom at the right side indicates the relative energy distribution of the wave types in the respective frequency bands. The sum of all contributions in this plot is 1.

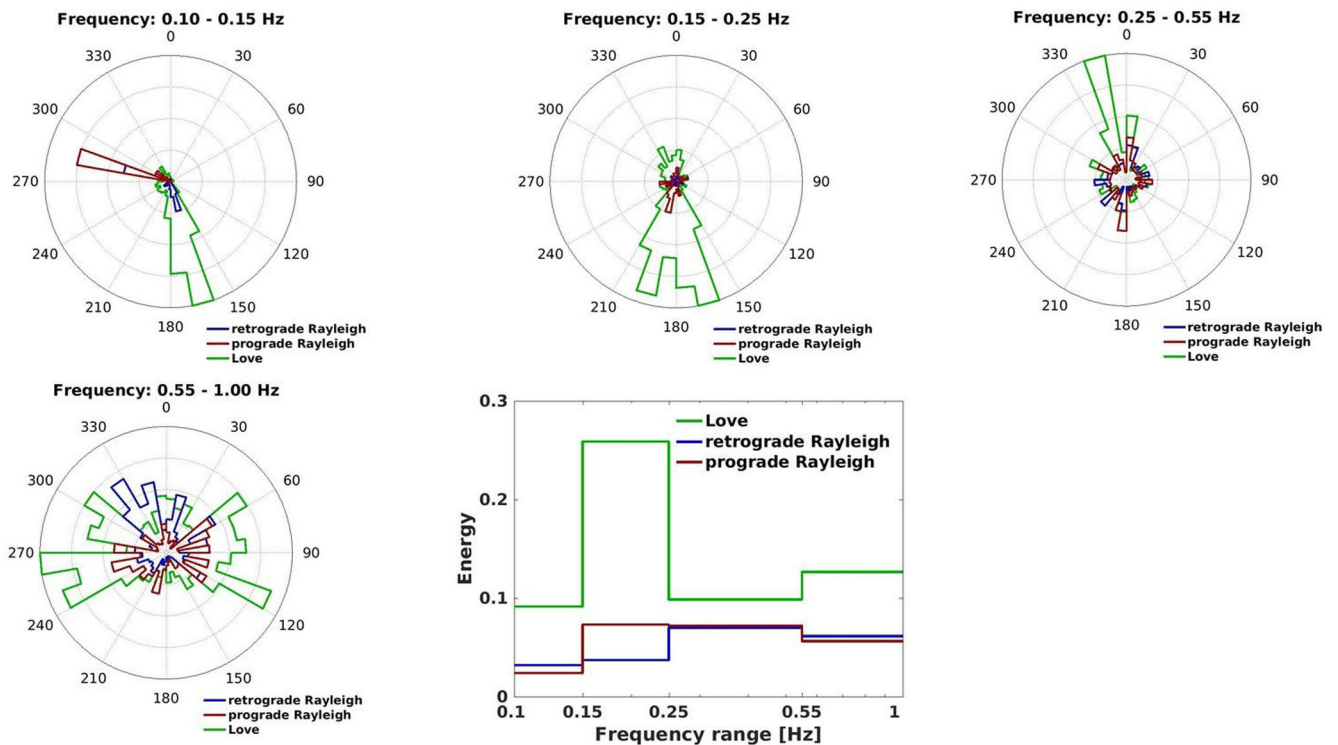


Figure 14. Azimuthal energy distribution for the scattered waves of all events stacked. The energy for each event was normalized by its total recorded energy. The plot on the bottom centre indicates the energy proportions of the different wave types in the different frequency ranges.

it also corresponds to the fundamental peak in the Rayleigh wave ellipticity and the fundamental peak in the *SH* transfer function (*S*-wave resonance). It is the most prominent wave in this frequency range observed during large (Vrancea 1977 event) and shallow earthquakes (event 351). In the *H/V* spectral ratio from ambient vibrations, the 0.25 Hz frequency corresponds to the most prominent peak (Manea *et al.* 2016).

A second notable frequency around 0.4 Hz corresponds to the Airy phase of the first higher mode of Love waves, but also to the first and second higher modes of the Rayleigh wave ellipticity and the second peak in the *SH* transfer function. It can be observed as a small bump in the *H/V* curve of ambient vibrations and as an increase of energy of Love waves in the earthquake wavefield. Moreover, the dispersion analysis also showed that only a small amount of energy was observed for this mode, especially in the ambient vibration wavefield (Manea *et al.* 2016).

The third particular frequency around 0.7 Hz corresponds to the peak of the third higher mode of Rayleigh wave ellipticity, the Airy phase of the second higher mode of Love waves and the third peak of the *SH* transfer function. It was detected in the *H/V* curves from ambient vibrations with relatively low amplitude. Bala (2013) interpreted it as the resonance of the interface between Quaternary and Neogene units. As already shown by Manea *et al.* (2016) and confirmed here, the whole profile down to the bedrock is actually necessary to interpret this frequency peak, not only the Quaternary sediments. It would even correspond to a shallower interface than Quaternary/Neogene. However, for most of the events, only a low amount of energy could be attributed to surface waves at this frequency. For some events (135, 140), Love waves contribute to a significant part to the wavefield energy. But unlike the fundamental mode, one cannot attribute the amplified ground motion at this frequency to the Airy phase of Love waves only.

A 3-D numerical model, based on the velocity structure used here, should be able to explain the distribution of energy at these three peak frequencies.

6 CONCLUSIONS

In this study, the seismic wavefield recorded in Bucharest was analysed. Bucharest is located on a sedimentary deposit spread out over the entire Moesian Platform. We could identify patterns and quantify the contribution of different seismic surface waves, such as the ones produced at the edges of this large sedimentary basin or multipath interference waves (Airy phases of Love and Rayleigh waves) on ground motion.

The spectral content of different types of events (shallow and intermediate depth) highlights the generation of surface waves with energy peaks around three distinct frequencies (0.16, 0.4 and 0.7 Hz). The first corresponds to the fundamental mode of the structure and the seismic energy is mostly due to the Airy phase of Love waves. The second frequency band corresponds to the first and second higher modes of Rayleigh and first higher mode of Love waves and the second peak in the *SH* transfer function and cannot be explained in a simple way. The domination of Love waves around the fundamental frequency may also hold under ambient vibrations, implying that the *H/V* curve cannot be used here as a proxy for Rayleigh wave ellipticity in this frequency range.

Around the fundamental frequency of the basin (0.15–0.25 Hz), the energy distribution of all 19 studied events shows dominating

Love waves arriving from their respective backazimuth. A significant scattering corresponding to 2-D or 3-D effects of the Moesian Platform, primarily coming from the southern and northern edges of the basin was observed. These reflected waves arrive at the array with less energy than the ones coming from the event's direction.

We investigated surface wave dispersion curves down to 0.1 Hz, corresponding to several kilometres of depth and retrieved information about the ellipticity curves. For almost all events, it was possible to retrieve the Love wave dispersion curves of the fundamental and higher modes. Combining the information from all earthquakes, the Love and Rayleigh wave dispersion curves and the Rayleigh wave ellipticity curves were successfully retrieved. The computed Love wave dispersion curves are in agreement with the ones obtained from ambient vibrations (Manea *et al.* 2016) and with the ones obtained by Sèbe *et al.* (2009) using regional earthquakes. Using earthquakes, the dispersion curves were retrieved with higher resolution: the first higher mode of Rayleigh waves was successfully captured and an improvement in resolution of the dispersion curves at higher frequency for the fundamental mode and higher modes was achieved. These results from MUSIQUE are also in agreement with the theoretical dispersion curves and ellipticity computed from the velocity profile proposed by Manea *et al.* (2016).

The characterization of the wavefield and its interpretation are important steps for the definition of the basin geometry for numerical simulations. The features of the seismic wavefield that were identified in this study help us to understand the variability of the ground motion recorded in Bucharest. It showed that the whole Moesian platform and especially its Northern and Southern edges should be modelled to be able to reproduce the observed low-frequency ground motion. Based on the results presented above, a 3-D geological model of the Moesian Platform will be developed and will be used to perform numerical simulations of the 3-D wave propagation from the Vrancea intermediate-depth seismic source to the Bucharest area. This model should be able to reproduce our observations, especially the generation of the low-frequency surface waves during large Vrancea earthquakes.

ACKNOWLEDGEMENTS

This study was performed in the framework of Sciex-NMS ch Programme (www.sciex.ch), SEER Project PN-III-P2–2.1-PED-2016–1014 and the PhD project of Elena Florinela Manea.

We are grateful to the editor, Dr Lapo Boschi, and to the anonymous reviewers for their remarks and valuable suggestions, which helped us to improve the quality of this paper.

The software suite ArcGis (www.esri.com/software/arcgis, last accessed 15 October 2016) has been used for this study.

REFERENCES

- Asch, K., 2003. The 1:5 million international geological Map of Europe and adjacent areas: development and implementation of a GIS-enabled concept, in *Geologisches Jahrbuch, SA 3*, E. Schweizerbart'sche Verlagsbuchhandlung, ed. Hannover.
- Auger, F. & Flandrin, P., 1995. Improving the readability of time-frequency and time-scale representations by the reassignment method, *IEEE Trans. Signal Process.*, **43**(5), 1068–1089.
- Bala, A., 2013. Modelling of seismic site amplification based on in situ geophysical measurements in Bucharest, Romania, *Romanian Rep. Phys.*, **65**(2), 495–511.

- Balan, S.F., Apostol, B.F. & Cioflan, C.O., 2011. Modeling geodynamical parameters for the local seismic effects estimation. Example for Galati and Tecuci Seismic Areas, *Rom. Rep. Phys.*, **63**(1), 240–249.
- Bonjer, K.P., Oncescu, M.C., Driad, L. & Rizescu, M., 1999. A note on empirical site responses in Bucharest, Romania, in *Vrancea Earthquakes: Tectonics, Hazard and Risk Mitigation*, pp. 149–162, eds Wenzel, F., Lungu, D. & Novak, O., Springer.
- Chávez-García, F.J., Stephenson, W.R. & Rodríguez, M., 1999. Lateral propagation effects observed at Parkway, New Zealand. A case history to compare 1D versus 2D site effects, *Bull. seism. Soc. Am.*, **89**(3), 718–732.
- Cioflan, C.O., Apostol, B.F., Moldoveanu, C.L., Panza, G.F. & Marmureanu, G., 2004. Deterministic approach for the seismic microzonation of Bucharest, *Pure appl. Geophys.*, **161**, 1149–1164.
- Cornou, C. & Bard, P.Y., 2003. Site-to-bedrock over 1D transfer function ratio: an indicator of the proportion of edge-generated surface waves?, *Geophys. Res. Lett.*, **30**(9), 1453, doi:10.1029/2002GL016593.
- Fäh, D., Suhadolc, P., Mueller, St. & Panza, G.F., 1994. A hybrid method for the estimation of ground motion in sedimentary basins: quantitative modeling for Mexico city, *Bull. seism. Soc. Am.*, **84**(2), 383–399.
- Fäh, D., Stamm, G. & Havenith, H.B., 2008. Analysis of three-component ambient vibration array measurements, *Geophys. J. Int.*, **172**, 199–213.
- Field, E.H., 1996. Spectral amplification in a sediment-filled valley exhibiting clear basin-edge-induced waves, *Bull. seism. Soc. Am.*, **86**(4), 991–1005.
- Frankel, A., Carver, D., Cranswick, E., Bice, T., Sell, R. & Hanson, S., 2001. Observations of basin ground motion from a dense seismic array in San Jose, California, *Bull. seism. Soc. Am.*, **91**, 1–12.
- Greco, B., Popa, M. & Radulian, M., 2003. Seismic ground motion characteristics in the Bucharest area: sedimentary cover versus seismic source control, *Rom. Rep. Phys.*, **55**(3), 322–331.
- Hanks, T.C., 1975. Strong ground motion of the San Fernando, California, earthquake: ground displacements, *Bull. seism. Soc. Am.*, **65**(1), 193–225.
- Hobiger, M., 2011. Polarization of surface waves: characterization, inversion and application to seismic hazard assessment, *PhD thesis*, Université de Grenoble, France.
- Hobiger, M., Cornou, C., Bard, P.-Y. & Le Bihan, N., 2011. MUSIQUE: A quaternion-based array processing technique for surface wave polarization analysis, in *IEEE Workshop on Statistical Signal Processing (SSP2011)*, Nice, France.
- Hobiger, M., Le Bihan, N., Cornou, C. & Bard, P.-Y., 2012. Multicomponent signal processing for rayleigh wave ellipticity estimation application to seismic hazard assessment, *IEEE Signal Process. Mag.*, **29**(3), 29–39.
- Hobiger, M., Cornou, C., Bard, P.-Y. & Le Bihan, N., 2016. Analysis of seismic waves crossing the Santa Clara Valley using the three-component MUSIQUE array algorithm, *Geophys. J. Int.*, **207**(1), 439–456.
- Imtiaz, A., Cornou, C., Bard, P.-Y., Zerva, A. & Hobiger, M., 2014. Diffracted wave field and coherency analysis: an example from dense array network in Argostoli basin, Cephalonia, Greece, in *Second European Conference on Earthquake Engineering and Seismology 24–29 August 2014, Istanbul, Turkey*.
- Joyner, W.B., 2000. Strong motion from surface waves in deep sedimentary basins, *Bull. seism. Soc. Am.*, **90**(6B), S95–S112.
- Konno, K. & Ohmachi, T., 1998. Ground-motion characteristics estimated from spectral ratio between horizontal and vertical components of microtremor, *Bull. seism. Soc. Am.*, **88**(1):228–241.
- Lebrun, B., Hatzfeld, D. & Bard, P.Y., 2002. Site effect study in urban area: experimental results in Grenoble (France), in *Earthquake Microzonation*, pp. 2543–2557, eds Roca, A. & Oliveira, C., Birkhäuser.
- Mandrescu, N., Radulian, M. & Marmureanu, G., 2007. Geological, geophysical and seismological criteria for local response evaluation in Bucharest urban area, *Soil Dyn. Earthq. Eng.*, **27**, 367–393.
- Manea, E.F., Michel, C., Poggi, V., Fäh, D., Radulian, M. & Balan, F.S., 2016. Improving the shear wave velocity structure beneath Bucharest (Romania) using ambient vibrations, *Geophys. J. Int.*, **207**(2), 848–861.
- Marmureanu, G., Moldoveanu, C., Cioflan, C. & Apostol, B., 1999. The seismic earth response by considering nonlinear behavior of the soils to strong Vrancea earthquakes, in *Vrancea Earthquakes: Tectonics, Hazard and Risk Mitigation*, pp. 175–185, eds Wenzel, F., Lungu, D. & Novak, O., Springer.
- Marmureanu, G., Marmureanu, A., Manea, E.F., Toma-Danila, D. & Vlad, M., 2016. Can we use more classic seismic hazard analysis to strong and deep Vrancea earthquakes?, *Rom. J. Phys.*, **61**(3), 728–738.
- Matenco, L., Bertotti, G., Cloetingh, S.A.P.L. & Dinu, C., 2003. Subsidence analysis and tectonic evolution of the external Carpathian–Moesian Platform region during Neogene times, *Sedimentary Geology*, **156**(1), 71–94.
- Michel, C. & Guéguen, P., 2010. Time-frequency analysis of small frequency variations in civil engineering structures under weak and strong motions using a reassignment method, *Struct. Health Monit.*, **9**(2), 159–171.
- Miron, S., Le Bihan, N. & Mars, J.I., 2006a. Quaternion-MUSIC for vector-sensor array processing, *IEEE Trans. Signal Process.*, **54**(4), 1218–1229.
- Miron, S., Le Bihan, N. & Mars, J.I., 2006b. High resolution vector-sensor array processing based on biquaternions, in *2006 IEEE International Conference on Acoustics, Speech and Signal Processing, 2006. ICASSP 2006 Proceedings*, IEEE, Toulouse, France.
- Moldoveanu, C.L. & Panza, G.F., 2002. Vrancea source influence on local seismic response in Bucharest, in *Earthquake Microzonation*, Pageoph Topical Volumes, pp. 2407–2429, eds Roca, A. & Oliveira, C., Birkhäuser.
- Moldoveanu, C.L., Marmureanu, G., Panza, G.F. & Vaccari, F., 2000. Estimation of site effects in Bucharest caused by the May 30–31, 1990, Vrancea seismic events, in *Seismic Hazard of the Circum-Pannonian Region*, pp. 249–267, eds Panza, G.F., Radulian, M. & Trifu, C.-I., Birkhäuser.
- Olsen, K.B., Day, S.M., Minster, J.B., Cui, Y., Chourasia, A., Faerman, M. & Jordan, T., 2006. Strong shaking in Los Angeles expected from southern San Andreas earthquake, *Geophys. Res. Lett.*, **33**, L07305, doi:10.1029/2005GL025472.
- Panza, G.F. *et al.*, 2002. Realistic modeling of seismic input for megacities and large urban areas, (the UNESCO/IUGS/IGCP project 414), *Episodes*, **25**(3), 160–184.
- Poggi, V. & Fäh, D., 2010. Estimating Rayleigh wave particle motion from three-component array analysis of ambient vibrations, *Geophys. J. Int.*, **180**, 251–267.
- Radulian, M., Mandrescu, N., Panza, G.F., Popescu, E. & Utale, A., 2000. Characterization of seismogenic zones of Romania, in *Seismic Hazard of the Circum-Pannonian Region*, pp. 57–77, eds Panza, G.F., Radulian, M. & Trifu, C.-I., Birkhäuser.
- Ritter, J.R., Balan, S., Bonjer, K., Diehl, T., Forbriger, T., Marmureanu, G., Wenzel, F. & Wirth, W., 2005. Broadband urban seismology in the Bucharest metropolitan area, *Seismol. Res. Lett.*, **76**(5), 574–580.
- Roten, D., Fäh, D., Olsen, K.B. & Giardini, D., 2008. A comparison of observed and simulated site response in the Rhône valley, *Geophys. J. Int.*, **173**(3), 958–978.
- Schmidt, R.O., 1986. Multiple emitter location and signal parameter estimation, *IEEE Trans. Antennas Propag.*, **34**(3), 276–280.
- Sèbe, O., Forbriger, T. & Ritter, J.R., 2009. The shear wave velocity underneath Bucharest city, Romania, from the analysis of Love waves, *Geophys. J. Int.*, **176**:965–979.
- Takemura, S., Akatsu, M., Masuda, K., Kajikawa, K. & Yoshimoto, K., 2015. Long-period ground motions in a laterally inhomogeneous large sedimentary basin: observations and model simulations of long-period surface waves in the northern Kanto Basin, Japan, *Earth, Planets and Space*, **67**:33, doi:10.1186/s40623-015-0201-7.
- Tari, G., Dicea, O., Faulkerson, J., Georgiev, G., Popov, S., Stefanescu, M. & Weir, G., 1997. Cimmerian and Alpine stratigraphy and structural evolution of the Moesian Platform (Romania/Bulgaria), in *Regional and Petroleum Geology of the Black Sea and Surrounding Region*, AAPG Memoir, vol. 68, pp. 63–90, ed. Robinson, A.G., American Association of Petroleum Geologists.
- Ville, J., 1948. Théorie et applications de la notion de signal analytique, *Cables Transm.*, **2A**, 61–74.
- Ward, J.P., 1997. *Quaternions and Cayley Numbers: Algebra and Applications*, Kluwer.

Wigner, E., 1932. On the quantum correction for thermodynamic equilibrium, *Phys. Rev.*, **40**(5), 749–759.

SUPPORTING INFORMATION

Supplementary data are available at [GJI](#) online.

Figure S1. Azimuthal energy distribution for different frequency ranges for event 021. The grey dot indicates the theoretical back-azimuth of the event. In each frequency range, all curves were normalized to the maximum. Bottom right: relative energy distribution of the different wave types in the respective frequency bands.

Figure S2. Same as Fig. S1 for event 038.

Figure S3. Same as Fig. S1 for event 061.

Figure S4. Same as Fig. S1 for event 077.

Figure S5. Same as Fig. S1 for event 085.

Figure S6. Same as Fig. S1 for event 088.

Figure S7. Same as Fig. S1 for event 121.

Figure S8. Same as Fig. S1 for event 135.

Figure S9. Same as Fig. S1 for event 137.

Figure S10. Same as Fig. S1 for event 140.

Figure S11. Same as Fig. S1 for event 144.

Figure S12. Same as Fig. S1 for event 167.

Figure S13. Same as Fig. S1 for event 179.

Figure S14. Same as Fig. S1 for event 183.

Figure S15. Same as Fig. S1 for event 194.

Figure S16. Same as Fig. S1 for event 206.

Figure S17. Same as Fig. S1 for event 320.

Figure S18. Same as Fig. S1 for event 328.

Please note: Oxford University Press is not responsible for the content or functionality of any supporting materials supplied by the authors. Any queries (other than missing material) should be directed to the corresponding author for the paper.